# Switching between solid solution and two-phase regimes in the $Li_{1-x}Fe_{1-y}Mn_yPO_4$ cathode materials during lithium (de)insertion : combined PITT, in situ XRPD and electron diffraction tomography study

**Reference:**

Drozhhin Oleg A., Sumanov Visiliy D., Karakulina Olesia, Abakumov Artem M., Hadermann Joke, Baranov Andrey N., Stevenson Keith J., Antipov Evgeny V..- Switching between solid solution and two-phase regimes in the $Li_{1-x}Fe_{1-y}Mn_yPO_4$ cathode materials during lithium (de)insertion : combined PITT, in situ XRPD and electron diffraction tomography study

Electrochimica acta - ISSN 0013-4686 - 191(2016), p. 149-157

Full text (Publishers DOI): http://dx.doi.org/doi:10.1016/j.electacta.2016.01.018

**Switching between solid solution and two-phase regimes in the $Li_{1-x}Fe_{1-y}Mn_yPO_4$ cathode materials during lithium (de)insertion: combined PITT, in situ XRPD and electron diffraction tomography study**

Oleg A. Drozhzhin[1*], Vasiliy D. Sumanov[1], Olesia M. Karakulina[2], Artem M. Abakumov[1,2,3], Joke Hadermann[2], Andrey N. Baranov[1], Keith J. Stevenson[3], Evgeny V. Antipov[1]

[1]*Department of Chemistry, Moscow State University, 119991, Leninskie Gory 1-3, Moscow, Russia*
[2]*EMAT, University of Antwerp, Groenenborgerlaan 171, B-2020, Antwerp, Belgium*
[3]*Skolkovo Institute of Science and Technology, 143025 Moscow, Russia*

* - Corresponding author

*E-mail* drozhzhin@hotmail.com

*Tel.* + 7 495 939 34 90, *Fax* + 7 495 939 47 88.

**Abstract**

The electrochemical properties and phase transformations during (de)insertion of $Li^+$ in $LiFePO_4$, $LiFe_{0.9}Mn_{0.1}PO_4$ and $LiFe_{0.5}Mn_{0.5}PO_4$ are studied by means of galvanostatic cycling, potential intermittent titration technique (PITT) and *in situ* X-ray powder diffraction. Different modes of switching between the solid solution and two-phase regimes are revealed which are influenced by the Mn content in $Li_{1-x}Fe_{1-y}Mn_yPO_4$. Additionally, an increase in electrochemical capacity with the Mn content is observed at high rates of galvanostatic cycling (10C, 20C), which is in good agreement with the numerically estimated contribution of the solid solution mechanism determined from PITT data. The observed asymmetric behavior of the phase transformations in $Li_{1-x}Fe_{0.5}Mn_{0.5}PO_4$ during charge and discharge is discussed. For the first time, the crystal structures of electrochemically deintercalated $Li_{1-x}Fe_{0.5}Mn_{0.5}PO_4$ with different Li content - $LiFe_{0.5}Mn_{0.5}PO_4$, $Li_{0.5}Fe_{0.5}Mn_{0.5}PO_4$ and $Li_{0.1}Fe_{0.5}Mn_{0.5}PO_4$ - are refined, including the occupancy factors of the Li position. This refinement is done using electron diffraction tomography data. The crystallographic analyses of $Li_{1-x}Fe_{0.5}Mn_{0.5}PO_4$ reveal that at x = 0.5 and 0.9 the structure retains the *Pnma* symmetry and the main motif of the pristine x = 0 structure without noticeable short range order effects.

**1. Introduction**

Despite the worldwide application and well-known attractive features of the $LiFePO_4$ cathode material [1], there are still some serious drawbacks which require further improvements. The relatively low working potential of $LiFePO_4$ - 3.43 V vs. $Li/Li^+$ - limits its theoretical specific energy (583 Wh $kg^{-1}$ in case of the Li anode), and the first-order phase transition between lithiated and delithiated phases reduces its specific power. The specific energy and specific power could be improved by partial substitution of Fe by Mn. First, the $Mn^{2+}/Mn^{3+}$ redox pair in $LiMnPO_4$ exhibits higher working potential of 4.1 V vs. $Li/Li^+$; and second, a significant amount of $Li^+$ (de)intercalates in $Li_{1-x}(Fe,Mn)PO_4$ olivines via a solid solution mechanism[2-10], thus enhancing the specific power (rate capability). The contribution of both single-phase and two-phase regions in $Li_{1-x}(Fe,Mn)PO_4$ during $Li^+$ extraction and insertion has been the subject of several recent studies but still remains a matter of debate [2-10].

According to the earlier works of Yamada et al. [2-4], the oxidation/reduction of the Mn cations in $Li_{1-x}Fe_{1-y}Mn_yPO_4$ during (de)lithiation always proceeds via two-phase reaction, while the $Fe^{2+}/Fe^{3+}$ redox pair is typically responsible for the solid solution behavior, and the width of the single-phase region

depends on Fe/Mn ratio. Malik et al. reported on the x-y-T phase diagram obtained from first-principles calculations [5], concluding that at room temperature a) for small Mn content ($y \leq 0.3$) the oxidation/reduction of Mn cations should occur through the solid-solution mechanism, and b) in case of $y = 0.5$ oxidation/reduction of both Fe and Mn cations takes place for *ca*. $0.4 \leq x \leq 0.6$.

Lack of crystal structure information on electrochemically deintercalated samples is one of the obstacles that prevent understanding of the transformations during charge-discharge. Since the quality of the *in situ* and *ex-situ* XRPD and neutron diffraction (ND) patterns of the charged samples do not allow a reliable Rietveld refinement, the majority of structure data presented in literature is theoretical [11,12] or corresponds to chemically deintercalated samples [4,13-17]. To our knowledge, only the structure of $FePO_4$, obtained electrochemically during an *in situ* ND experiment, was reported [18,19].

In an effort to elucidate the solid solution and two phase (de)insertion mechanisms, we performed potentiostatic intermittent titration tests (PITT) in combination with *in situ* X-ray powder diffraction (XRPD) and the refinement of three selected $Li_{1-x}Fe_{0.5}Mn_{0.5}PO_4$ crystal structures from electron diffraction tomography (EDT) data. While the existence of a broad range of solid solution for $Li_{1-x}Fe_{0.5}Mn_{0.5}PO_4$ (or close compositions) was confirmed by *in situ* X-ray powder diffraction in a number of works [7-10], to our knowledge, there has been no detailed experimental study for olivines with low Mn content, which, according to [5] and contrary to [2-4], should exhibit single-phase behavior in the $Mn^{2+}/Mn^{3+}$ region. In the present work we provide combined comparative studies of the single-phase contribution by *in situ* XRPD, EDT and numerical approximation using accurate electrochemical investigation for three different materials: $LiFePO_4$ and two compositions with different Fe:Mn ratio, namely $LiFe_{0.9}Mn_{0.1}PO_4$ and $LiFe_{0.5}Mn_{0.5}PO_4$.

## 2. Experimental

Carbon-coated particles of $LiFe_{1-y}Mn_yPO_4$ ($y = 0, 0.1, 0.5$) were synthesized via hydrothermal route. We used $FeSO_4 \times 7H_2O$, $MnSO_4 \times 5H_2O$, $H_3PO_4$ (85%) and $LiOH \times H_2O$ in the molar ratio (Fe+Mn):P:Li = 1:1:3, respectively, as starting materials, and 5 g of ascorbic acid per 1 mol of d-cations as a reducing agent. The precursor solutions (first with LiOH, and second with other reagents) were prepared by dissolving stoichiometric amounts of reactants in deionized and degassed water. Solutions were heated to 80°C and stirred for 5 min, then mixed with a formation of gel (pH ~ 9.5-10), which was placed in a Teflon vessel and sealed tightly in a stainless-steel autoclave (fill factor 0.85). The autoclave was heated to 200°C and kept at this temperature for three hours, and then it was cooled down to room temperature. The resulting precipitate was centrifuged three times (6000 rpm, 3 min) in distilled water, filtered and dried at room temperature. The powder was ball-milled in a planetary mill (220 rpm, 1 h) with 30 wt.% of d-glucose under ethanol, dried and annealed at 600°C for 1 h in the atmosphere of $Ar/H_2$ (95:5) to provide carbon coating on the $LiFe_{1-y}Mn_yPO_4$ particles. The carbon content in $LiFe_{1-y}Mn_yPO_4/C$ (appr. 10% wt.) was determined by the termogravimetric analysis.

The phase composition of the obtained samples was characterized by X-ray powder diffraction (XRPD) (Huber Guinier camera G670 with an ImagePlate detector, $CuK_{\alpha 1}$ radiation). The pattern fitting and refinement of the lattice parameters were performed using the WinXpow program suite. The determination of size and morphology of the particles, together with EDX measurements, was carried out using scanning electron microscopy (SEM) (Carl Zeiss NVision 40-38-50).

Electrochemical measurements were carried out in two-electrode cells. To form the working electrode, a carbon-coated composite material ($LiFe_{1-y}Mn_yPO_4/C$) was mixed with conductive carbon black (Timcal Super-C) and polyvinylidene fluoride in 75:15:10 ratio, respectively. The dry mixture was mixed with N-methyl pyrrolidon; resulting slurry was applied on Al foil with the “doctor blade” technique and then dried at 75°C for 3 h. Dried electrodes were rolled, punched to round discs and dried at 120°C for 3 h under dynamic vacuum. Electrochemical cells were assembled in MBraun glove box under Ar atmosphere. The electrolyte used for the measurements contained 1 M $LiPF_6$ in ethylene

carbonate (EC) and dimethyl carbonate (DMC) solution with 1:1 volume ratio. Potentiostat-galvanostat Biologic VMP-3 (EC-Lab software) was used for data collection. Three electrochemical techniques were used: GCPL (galvanostatic cycling with potential limitation), PITT (potentiostatic intermittent titration technique) and CV (cyclic voltammetry). For GCPL experiments, the cell was cycled between 2.2 and 4.3 V vs. $Li/Li^+$ at 0.05C-20C rate. PITT measurements were performed at potentials 2.2 V - 4.3 V (vs. $Li/Li^+$), with 10 mV steps and 0.01C current cutoff. CV experiments were performed within the same potential range at 50 $\mu V\ s^{-1}$ scan rate.

*In situ* XRPD studies were performed with a Bruker D8 Advance diffractometer (reflection mode, Cu$K_{\alpha 1}$ radiation, LynxEye PSD) in a self-made electrochemical cell containing a Be window at the anode (Li) side. XRPD data in a narrow $2\Theta$ angular range ($28\text{-}33^o$) were collected every 30 min (duration of data collection – appr. 10 min) during GCPL experiments at 0.1C rate. *Ex situ* XRPD investigation was carried out with a STOE STADI P diffractometer ($CoK_{\alpha 1}$ radiation, transmission mode, curved Ge(111) monochromator, linear PSD).

Specimens for transmission electron microscopy were prepared by crushing the samples in a mortar under dry hexane and depositing a few drops of the suspension onto a holey carbon film supported by a Cu grid. The specimens of pristine $LiFe_{0.5}Mn_{0.5}PO_4$ were prepared in air, whereas the specimens of the materials charged to 3.7 V vs. $Li/Li^+$ and 4.2 V vs. $Li/Li^+$ were prepared in an Ar-filled glove box and transported to the microscope column completely excluding contact with air. Selected area electron diffraction (SAED) studies and electron diffraction tomography (EDT) experiments were performed using Tecnai G2 and Tecnai Osiris transmission electron microscopes operated at 200 kV. The EDT experiments were performed by manually collecting reciprocal lattice sections with an angular step of $1^o$. More details on the collected EDT data can be found in Table S1 of the Supporting Information. Difference vector space analysis, indexing and integration of the reflection intensities were performed with the PETS and JANA2006 software [20,21]. Crystal structure refinement from XRPD and EDT data was performed with JANA2006.

## 3. Results

### *3.1. Samples characterization*

The XRPD patterns of the three studied samples ($LiFePO_4$, $LiFe_{0.9}Mn_{0.1}PO_4$ and $LiFe_{0.5}Mn_{0.5}PO_4$) are presented in Fig. 1. The patterns do not contain any visible peaks of impurities and can be indexed in an orthorhombic unit cell (S.G. *Pnma*). Lattice parameters, calculated from XRPD data, are summarized in Table 1.

An increase in unit cell volume occurs for both Mn-substituted materials (290.21 $Å^3$ for $LiFe_{0.9}Mn_{0.1}PO_4$ and 294.92 $Å^3$ for $LiFe_{0.5}Mn_{0.5}PO_4$), which is in good agreement with Vegard's law for solid solutions and with previously reported data [2-4].

SEM image (inset in Fig. 1) illustrates the typical plate-like morphology of the obtained samples before carbon coating. Substitution of $Fe^{2+}$ by $Mn^{2+}$ does not affect particle size or shape. All samples are composed of thin crystallites with an average thickness about 150-200 nm and lateral dimensions of 1-2 µm. Previously reported data [22] indicate that direction with the smallest thickness of the particles obtained via hydrothermal synthesis corresponds to the [010] direction of the unit cell in the *Pnma* setting and coincides with the diffusion path of $Li^+$ ion in olivine-type cathodes.

### *3.2. Electrochemical measurements*

The results of the GCPL measurements for the studied materials are presented in Fig. 2.

GCPL discharge curves collected at 0.05C rate (Fig. 2a) indicate approximately the same electrochemical capacity close to 140 mAh $g^{-1}$ for $LiFePO_4$, $LiFe_{0.9}Mn_{0.1}PO_4$ and $LiFe_{0.5}Mn_{0.5}PO_4$. The samples demonstrate different behavior of the E-C dependence. $LiFePO_4$ has an almost flat plateau at

*ca.* 3.4 V vs. $Li/Li^+$, while $LiFe_{0.5}Mn_{0.5}PO_4$ shows two plateaus (at 3.5 and 4.0 V vs. $Li/Li^+$) with a rather long drawn out slope in between.

As it was shown previously [8], this intermediate region corresponds to simultaneous redox transitions of $Fe^{2+}/Fe^{3+}$ and $Mn^{2+}/Mn^{3+}$ suggesting a) random occupation of d-metal position in olivine structure by Fe and Mn cations and b) homogeneous distribution of Fe and Mn in the crystallites. The discharge curve of $LiFe_{0.9}Mn_{0.1}PO_4$ does not demonstrate any significant contribution at high potential (4.0 V vs. $Li/Li^+$), but does contain the same slope between 4.0 and 3.5 V vs. $Li/Li^+$ corresponding to the capacity of 10-15 mAh $g^{-1}$. The rate performance of the studied samples (Fig. 2b) revealed increasing electrochemical capacity at high discharge rates (10C, 20C) with the Mn content. It should be noted that increasing the current density brings the electrochemical system from a kinetic-controlled state to diffusion-controlled state, therefore at 10C-20C rates such factors as composite conductivity, electrode thickness, charge transfer resistance etc. have much less impact on the measured electrode performance than the mechanism of $Li^+$ (de)insertion and the solid state diffusion rates. As the samples were synthesized in the same experimental conditions and have the same morphology, the observed increase in capacity can be attributed to changes in the mechanism of $Li^+$ (de)insertion. To clarify this, we performed PITT, *in situ* XRPD and EDT studies. These independent experimental methods can help to reveal the nature of the phase transformations in the $Li_{1-x}MPO_4$ system with different Mn/Fe ratio.

Raw PITT data (I-t and E-t plots) for the three studied samples are presented in Fig. S1. Details of the processing of the PITT data are also presented in Supporting information.

In general, the I(t) dependence in case of a diffusion-controlled process at planar electrodes should follow the classical Cottrell equation based on Fick's laws [23]. However, Montella in his computational work proposed a more elaborated theory which took into account the ohmic potential drop and/or the slow kinetics of the interfacial $Li^+$ ion transfer across the electrode/electrolyte interface [24]. Based on this work, Vorotyntsev, Levi and Aurbach proposed several analytical expressions for describing the I(t) dependence in the short-time region [25]. One of these expressions was elaborated further by Meethong et al. for division of the charge passed through the cell into "diffusion" and "two-phase" contributions [26].

The "diffusion" part of the charge – $f\ \Delta Q$ - corresponds to the amount of Li (de)inserted in the cathode material by solid solution (or single-phase) mechanism only, without phase transition. Subsequently, evaluating *f*-values for compositions with different Li content, we can estimate total contribution of the single-phase mechanism into the overall $Li^+$ extraction-insertion process ($f$ = 0 indicates two-phase reaction, and $f$ = 1 corresponds to ideal solid solution). The *f*-x dependence for $Li_{1-x}MPO_4$, obtained after treatment of the PITT data, is displayed in Fig. 3.

It is clearly seen that the amount of "diffusion" charge passed during the PITT experiments increases with Mn content. Total average values $f_{sum} = \sum(f\ \Delta Q) / \sum(\Delta Q)$ for the three samples for the whole studied potential range are listed in the Table 2. Two conclusions can be made from the results presented in the Table 2:

a) the amount of charge, associated with the single-phase mechanism of $Li^+$ (de)insertion, $– f_{sum} –$ is higher for $Li^+$ insertion process, and it is the most apparent for the $LiFePO_4$ sample. Similar results for the undoped $LiFePO_4$ were obtained in [26]. Authors explained their observations with differences in geometrical or morphological configuration of phases during charge and discharge. We believe that the different length of solid solution regions for Li-poor and Li-rich phases, as well as the difference in electronic and ionic conductivity of these phases, also may influence on the process of nucleation and growth of the corresponding phases, thus resulting in different $f_{sum}$ values for the charge and discharge processes.

b) $f_{sum}$ increases with Mn content. Most probably, the increasing of the overall length of the solid solution regions in Mn-substituted samples is the reason of the lower difference in $f_{sum}$ values for anodic and cathodic processes.

To verify the scenario of the phase transformations obtained by PITT, we investigated the evolution of the crystal structure across the phase transitions.

### *3.3. In situ X-ray powder diffraction study*

We performed an *in situ* XRPD study to obtain direct information about the phase transformations in the studied samples during extraction-insertion of $Li^+$. We selected a short range of 2Θ angles – 28-33$^o$ – which contain intense peaks ((211)/(020) and (301)) of the initial olivine diffraction pattern, which undergo significant changes during charge ($Li^+$ deinsertion) and discharge ($Li^+$ insertion) of the materials. The selected regions of the *in situ* XRPD patterns for the studied samples are presented in Fig. 4.

For the further treatment of the experimental data, we assumed that continuous change of the position of the peaks in the XRPD pattern without major change in intensity during charge or discharge testify to existence of the solid solution region; while substantial variation of intensity of the peaks at the different 2Θ angles without significant shift of their position corresponds to two-phase region.

Thereby, the samples demonstrate different behavior depending on the Mn content:

1) For the undoped $LiFePO_4$ sample, almost the whole process of $Li^+$ extraction/insertion occurs through a two phase (de)insertion mechanism ($LiFePO_4$ - LFP - and $FePO_4$ - FP) without a significant shift of diffraction peaks (and, correspondingly, with practically constant unit cell parameters of both phases)

2) For the $LiFe_{0.9}Mn_{0.1}PO_4$ sample, a significant contribution of the single-phase mechanism appears (see red arrows on the Fig. 4b). We also observe two phases here, but the Li-deficient phase exhibits a solid solution region $Li_{1-x}Fe_{0.9}Mn_{0.1}PO_4$ ($L_{1-x}$FMP) for $0.8 \le x \le 1$. Phase transformation during charge and discharge are in a good accordance with each other.

3) For the $LiFe_{0.5}Mn_{0.5}PO_4$ sample, three phases appear during Li (de)insertion: LFMP, $L_{1-x}$FMP and FMP. The whole charge process is split into three regions:

two-phase region between LFMP and $L_{1-x}$FMP, solid solution $L_{1-x}$FMP, two-phase region between $L_{1-x}$FMP and FMP.

At discharge, the same switching between two-phase and single-phase modes occurs, but a noticeable increase in the extent of the single-phase region is detected (the transition between the $L_{1-x}$FMP solid solution and $L_{1-x}$FMP-LFMP two-phase region is smeared out).

A clear asymmetry between charge and discharge behavior of the system, which is appeared as a visible difference in the extension of the sloped region, is also evident from the form of the E-x curves obtained by PITT, GCPL at 0.2C rate and CV experiments shown in Fig. 5. However, in case of the PITT experiment this difference is not so remarkable.

### *3.4. Crystal structures of $Li_{1-x}Fe_{0.5}Mn_{0.5}PO_4$ at different charged state*

In order to get a better insight into the structural transformation occurring in $LiFe_{0.5}Mn_{0.5}PO_4$ upon $Li^+$ extraction the crystal structure refinements of the of three representative samples were performed (the pristine sample, the mid-charged (3.7 V vs. $Li/LI^+$) sample from the solid solution region and the sample from the two-phase region at the end of charge (4.2 V vs. $Li/LI^+$)). The quality of the *in situ* and *ex-situ* XRPD patterns of the charged samples does not allow a reliable Rietveld refinement. Thus, electron diffraction tomography (EDT) was chosen as the method for the crystallographic study. Earlier we have demonstrated that quantitative electron diffraction in a precession mode can be used for the

determination and refinement of the crystal structures of $Li_2CoPO_4F$ (high voltage cathode material) and $LiBH_4$ (light weight borohydride for hydrogen storage) and demonstrated the ability of electron diffraction to detect such "light" element as Li and provide reliable crystallographic information [27,28]. Compared to precession electron diffraction, electron diffraction tomography provides a more complete coverage of the reciprocal space and allows collecting 3D datasets of quasi-kinematical electron diffraction intensities, which are suitable for the structure solution and refinement [29].

Conventional SAED patterns were collected for the pristine and charged samples in order to verify their unit cell and space group (Fig. 6). All the patterns can be indexed on the same primitive orthorhombic lattice with the unit cell parameters $a$ ~ 10Å, $b$ ~ 6Å, $c$ ~ 4.8Å. The low precision in the interplanar spacing measurement does not allow unambiguous detection of variation of the unit cell parameters upon Li extraction. The reflection conditions 0$kl$: $k$+$l$ = 2n and $hk$0: $h$ = 2n are observed for all three samples, in agreement with the space group *Pnma*. Thus, one can conclude that neither the unit cell metrics nor the space symmetry change upon Li extraction from $LiFe_{0.5}Mn_{0.5}PO_4$. The SAED patterns do not show structured diffuse scattering, thus there is no sign of short range order. The exact values of the unit cell parameters were extracted from *ex-situ* XRPD data using LeBail fit and are summarized in Table S1 of the Supporting Information. The $a$ and $b$ parameters decrease concomitantly with the Li content, whereas the $c$ parameter demonstrates a slight enlargement. This behavior generally agrees with the literature data on the compositions with close Mn/Fe ratio (i.e. $Li_{1-x}Fe_{0.4}Mn_{0.6}PO_4$, $Li_{1-x}Fe_{0.6}Mn_{0.4}PO_4$) [2,7,9]. The transition from the pristine state to the 3.7 V charged state is accompanied by a relatively small unit cell volume decrease of ~1.6%, whereas upon the transition from 3.7 V to 4.2 V charged states the volume decrease is significantly larger (~6.7%), correlating well with the volume changes observed by Ravnsbæk *et al* with synchrotron XRPD [10].

The reliability of the structure solution from the EDT data was verified by comparing the refined crystallographic parameters of pristine $LiFe_{0.5}Mn_{0.5}PO_4$ with those from the Rietveld refinement from XRPD data (the details on the refinement procedures are provided in Supporting Information, the crystallographic and structural parameters are listed in Tables S1-S3; the $F_{obs}$-$F_{calc}$ plots are shown in Fig. S2). The atomic coordinates and interatomic distances obtained with both methods are very similar and the bond valence sums (BVS) for the (Fe,Mn), Li and P positions are chemically sensible. The (Fe,Mn) – O separations are obviously an effective average between the larger $Mn^{2+}$ - O (r($Mn^{2+}$) = 0.83 Å) and smaller $Fe^{2+}$ - O (r($Fe^{2+}$) = 0.78 Å) interatomic distances. This is indicated in the underestimated BVS value for the (Fe,Mn) position if it is calculated with the $B$ and $R_0$ parameters (s = $e^{(R-Ro)/B}$, $s$ – valence, $R$ - interatomic distance) for $Fe^{2+}$ and overestimated BVS if the parameters for $Mn^{2+}$ are used. Similar to the $LiFePO_4$ structure [27], the (Fe,Mn)$O_6$ octahedra are noticeably distorted, with three shorter (~2.07 – 2.12Å) and three longer (~2.22 – 2.25 Å) (Fe,Mn)-O distances. The integral octahedral distortion parameter calculated as

$$\Delta d = 1/6 \sum_{n=1-6} \left[ \left( d_n - d \right) / d \right]^2,$$

where $d_n$ is an individual (Fe,Mn)-O bond length and $d$ is an average (Fe,Mn)-O bond length, scales to $\Delta d = 1.7 \cdot 10^{-3}$.

The difference Fourier map calculated from the EDT data around the Li position in $LiFe_{0.5}Mn_{0.5}PO_4$ while setting its occupancy factor to zero shows a clear peak of scattering density corresponding to the Li atom (Fig. 7a). The refined occupancy of the Li position is 0.94(6) corresponding within the standard deviation to the bulk chemical composition. For the sample delithiated at 4.2 V no scattering density is observed on the difference Fourier map (Fig. 7b) indicating that the Li position is nearly empty, in agreement with its refined occupancy factor 0.14(11). For the intermediate sample charged to 3.7 V, the Li position appears half populated, with the occupancy factor of 0.54(7). The refined occupancies are in excellent agreement with the Li contents measured from the *E-x* dependence obtained with the GCPL and PITT methods (Fig. 5a,b).

Upon delithiation, the BVS for the Fe and Mn cations steadily increases (see Table S3). For $Li_{0.5}Fe_{0.5}Mn_{0.5}PO_4$ the BVS values calculated with the parameters for $Fe^{3+}$ and $Mn^{2+}$ appear strongly underestimated (2.09 for $Fe^{3+}$) and overestimated (2.27 for $Mn^{2+}$), respectively. Taking into account that at 3.7 V the Fe atoms are mainly oxidized to $Fe^{3+}$, whereas the majority of the Mn atoms are still in the $Mn^{2+}$ state, this BVS reflects large local strain in the structure. The average (Fe,Mn)-O distance is too long for the relatively small $Fe^{3+}$ cations ($r(Fe^{3+})$ = 0.645 Å) causing strong apparent underbonding and at the same time it is too short of for the $Mn^{2+}$ cation causing their apparent overbonding. One may assume that this bonding mismatch is at least partially relieved by local displacements of the oxygen atoms resulting in the strained structure. In the $Li_{0.1}Fe_{0.5}Mn_{0.5}PO_4$ structure this strain is relaxed because the $Fe^{3+}$ and $Mn^{3+}$cations have the same ionic radii ($r(Fe^{3+})$ = 0.645 Å). These results in the BVS value of 2.6 for the Fe and Mn cations that approaches the value expected from the refined Li content (2.86).

Finally, the crystallographic data on the $Li_{1-x}Fe_{0.5}Mn_{0.5}PO_4$ material with different Li content allowed us to verify the role of the cooperative Jahn-Teller distortion due to $Mn^{3+}$ in the delithiation mechanism. On going from $LiFe_{0.5}Mn_{0.5}PO_4$ to $Li_{0.1}Fe_{0.5}Mn_{0.5}PO_4$, the octahedral distortion parameter stays practically the same ($\Delta d = 1.7 \cdot 10^{-3}$ and $1.6 \cdot 10^{-3}$, respectively), i.e. oxidation of $Mn^{2+}$ to $Mn^{3+}$ does not introduce additional distortion into the $(Fe,Mn)O_6$ octahedra. This is in striking contrast with the octahedral distortion in delithiated compounds with higher Mn content. In the $Fe_{0.2}Mn_{0.8}PO_4$ and $MnPO_4$ compounds, the two bonds to the oxygen atoms forming a common edge with the $PO_4$ tetrahedra become substantially longer (up to 2.326 Å in $MnPO_4$), whereas the four other bonds get shorter (1.85 – 1.96 Å in $MnPO_4$) [30,31]. The octahedral distortion parameter scales to $7.9 \cdot 10^{-3}$ and $9.9 \cdot 10^{-3}$ for $Fe_{0.2}Mn_{0.8}PO_4$ and $MnPO_4$, respectively. This difference in octahedral distortion indicates that the Jahn-Teller deformation in $Li_{0.1}Fe_{0.5}Mn_{0.5}PO_4$ is not of cooperative nature and contributes mainly to the local structure distortion.

**4. Discussion**

As discussed previously, *f*-values derived from the PITT measurements for the compositions with different Li content, report on the total contribution of the single-phase mechanism to the overall $Li^+$ extraction-insertion process. As it can be seen from Fig. 3, the *f* - x dependence obtained from the PITT data is in a good agreement with the phase transformations behavior directly observed by *in situ* XRPD (Fig. 4). For $Li_{1-x}FePO_4$, *f* is close to 0 almost in the whole region of x, except narrow regions ($\Delta x \approx 0.05$) near $LiFePO_4$ (x = 0) and $FePO_4$ (x = 1) points. For $Li_{1-x}Fe_{0.9}Mn_{0.1}PO_4$, *f* is close to 0 at the x ≈ 0.05-0.85 region, indicating a two-phase process for oxidation/reduction of the Fe cations, and single-phase mechanism for that part of (de)insertion process, which corresponds to oxidation/reduction of Mn/Fe cations. For $Li_{1-x}Fe_{0.5}Mn_{0.5}PO_4$, *f* displays three maxima: at the beginning, at the end points (like for $LiFePO_4$), and in between. However, the difference between the onsets of phase transformation of $Li_{1-x}Fe_{0.5}Mn_{0.5}PO_4$ during extraction and insertion processes in case of the PITT experiment is smaller than in case of other electrochemical techniques used in our work. It was shown earlier [10] that enhancing the rate of $Li^+$ (de)insertion process leads to increasing of the amount of the solid solution mechanism, as the system moves far from equilibrium state. As the PITT technique brings the studied system closer to the equilibrium, we obtain the lowest observed contribution of the solid solution mechanism, and better match of the obtained parameters for $Li^+$ extraction and insertion processes. This assumption explains different forms of the E-x curves obtained with GCPL at 0.2C rate, CV at 50 $\mu V\ s^{-1}$ rate and PITT study (extraction and insertion of the overall $Li^+$ in $LiFe_{0.5}Mn_{0.5}PO_4$ took *ca.* 5, 4 and 50 hours, correspondingly), see Fig. 5.

Several conclusions may be made from these results.

An increase in solid solution contribution with the Mn content is observed. As a result, the discharge capacity at high (10-20C) rates presented in Fig. 2, also increases in the line $LiFePO_4$ - $LiFe_{0.9}Mn_{0.1}PO_4$ - $LiFe_{0.5}Mn_{0.5}PO_4$.

As it was computed earlier [5], the phase transformation behavior for the olivines with low Mn content (e.g. $LiFe_{0.9}Mn_{0.1}PO_4$) is different from undoped $LiFePO_4$ and the materials with higher substitution level (e.g. $LiFe_{0.5}Mn_{0.5}PO_4$). We have indeed not observed second two-phase state corresponding to $Mn^{2+}/Mn^{3+}$ redox pair for $Li_{1-x}Fe_{0.9}Mn_{0.1}PO_4$ in XRPD patterns. The *f*-values, corresponding to solid solution contribution, demonstrate almost the same properties: they close to 1 for x>0.8 (see Fig. 3b).

In spite of rather intensive studies of $LiFe_{0.5}Mn_{0.5}PO_4$ and close compositions ($Fe_{0.4}Mn_{0.6}$, $Fe_{0.6}Mn_{0.4}$), there is still no clear answer as to why asymmetric phase transformations are observed for delithiation and lithiation of this material (for sure, we mean phase transformation behavior under dynamic conditions). We point out that this aspect was noticed in at least three works [8-10] but not elaborated upon. Only Ravnsbæk and co-authors speculate that this effect was due to by non-symmetric character of coherency strains [10]. We propose a more straightforward explanation of the observed phase transformations in $Li_{1-x}Fe_{0.5}Mn_{0.5}PO_4$ based on three experimentally proven statements:

a) as revealed by SAED and EDT structure analysis in this work, the transformations upon changing the Li content are not associated with dramatic structural variations: the framework of the pristine *Pnma* structure is retained and the distortion of the $(Mn,Fe)O_6$ polyhedra almost does not change, contrarily to that can be expected from the presence of $Mn^{3+}$ cations demonstrating the Jahn-Teller effect;

b) the transformations are accompanied with significant changes in the unit cell volume. The $Mn^{2+}$ cation radius is larger than that of $Fe^{2+}$ in octahedral coordination (Shannon radii - 0.83 Å vs. 0.78 Å), but $Mn^{3+}$ radius is close to $Fe^{3+}$ one (0.645 Å) because of the Jahn-Teller effect for $Mn^{3+}$, as it was proposed by Yamada et al. [4]. This difference is the reason for the different volume changes for the undoped $LiMPO_4/MPO_4$ transitions: *ca*. 11% for M = Mn and 7% for M = Fe [2-4].

c) in the intermediate region of x (approx. $0.4<x<0.6$) in $Li_{1-x}Fe_{0.5}Mn_{0.5}PO_4$ simultaneous reduction and oxidation of Fe and Mn take place due to the random distribution of the Mn and Fe cations in the lattice, as it was demonstrated earlier by means of an *in situ* XANES study [8].

During charge, the Li extraction starts from a narrow single-phase region, where the concentration of the Li vacancies is accumulated to the level sufficient for a nucleation of the second $L_{1-x}FMP$ phase. Then, main fraction of $Fe^{2+}$ is oxidized to $Fe^{3+}$ during the two-phase process, similar to that in $LiFePO_4$. However, random distribution of Fe and Mn in the structure leads to appearance of a single-phase solid solution region. This explains that the transition to the second two-phase state (associated with $Mn^{2+}/Mn^{3+}$ redox pair) begins when some fractions of Mn ions are already oxidized, and average d-cation radius in $L_{1-x}FMP$ phase – and, correspondingly, the unit cell volume of the phase - is smaller than it would have been without the existence of the $L_{1-x}FMP$ solid solution. As a result, the volume change in the second phase transition is smaller than it would have been in the case of a pure $Mn^{2+}/Mn^{3+}$ redox reaction (as in $LiMnPO_4$, for example). However, after complete oxidation of both Fe and Mn cations, the average radius of the d-cations is 0.645 Å, and when lithiation (discharge) begins, the appearance of large $Mn^{2+}$ cations (0.83 Å) leads to a large volume change between FMP and $L_xFMP$ phases. As a result of the larger volume of the $L_xFMP$ phase, increasing the $Fe^{2+}$ concentration does not lead to high strain in the crystal lattice, and the contribution of the single-phase mechanism become larger than for the delithiation process.

According to this conjecture, we can propose a different phase transition mechanism for other double olivines. For example, for $Li_{1-x}Fe_{0.5}Co_{0.5}PO_4$ ($r(Co^{2+})$ – 0.74 Å, $r(Co^{3+})$ – 0.61 Å in octahedral coordination; volume change between $LiCoPO_4$ and $CoPO_4$ ≈ 7% [32]) most probably, one two-phase and one single-phase region should exist for both charge ($Li^+$ deinsertion) and discharge ($Li^+$ insertion).

The data published recently by Kosova et al. [33] partly confirms our assumption as the authors reported that solid solution mechanism occurs via whole range of x in $Li_xFe_{0.5}Co_{0.5}PO_4$ during $Li^+$ deinsertion (with more significant shift of peak positions in the intermediate region); however, additional *in situ* XRPD study on discharge is needed. In our opinion, another situation could be observed for the $Li_{1-x}Mn_{0.5}Co_{0.5}PO_4$ system, i.e. one two-phase region and one solid solution region at charge and two two-phase and one solid solution region at discharge - because in this case the Mn cations start to oxidize earlier at delithiation, and later – at lithiation. The form of CV curves presented, for example, by Ni et al. [34] supports our assumption, but a more accurate study of the $Li^+$ (de)insertion processes in this material is needed to draw more concrete conclusions.

## 5. Conclusions

Combined PITT and *in situ* XRPD experiments were used to study the phase transformations in the $Li_{1-x}FePO_4$, $Li_{1-x}Fe_{0.9}Mn_{0.1}PO_4$ and $Li_{1-x}Fe_{0.5}Mn_{0.5}PO_4$ cathode materials. Both methods revealed that the increase in the amount of single-phase contribution to the overall insertion mechanism tracts directly with the Mn content. These results are in a good accordance with the results obtained by galvanostatic cycling at high (up to 20C) rates which revealed a higher relative capacity for the Mn-substituted samples. The amount of the solid solution contribution is not equal for the deinsertion and insertion processes - it is larger during $Li^+$ insertion for all studied compounds. A simple explanation of the asymmetry of phase transformations behavior for Mn-substituted olvines is proposed which is based on the existence of the solid solution region together with different relative changes of ionic radii for $Fe^{2+}/Fe^{3+}$ and $Mn^{2+}/Mn^{3+}$ cations. This should also be evident for other related olivine materials such as $Li_{1-x}Fe_{0.5}Co_{0.5}PO_4$ and $Li_{1-x}Mn_{0.5}Co_{0.5}PO_4$.

**Supplementary materials**.

Contains detailed description of the processing of the PITT data, tables with refinement parameters, crystallographic data, atomic coordinates and selected interatomic distances for the $LiFe_{0.5}Mn_{0.5}PO_4$, $Li_{0.5}Fe_{0.5}Mn_{0.5}PO_4$ and $Li_{0.1}Fe_{0.5}Mn_{0.5}PO_4$ structures refined from EDT data.

**Acknowledgements**

This work was supported by the Russian Foundation of Basic Research (grants No. 14-29-04064 and 14-03-31473), Skolkovo Institute of Science and Technology, and the Lomonosov Moscow State University Program of Development.

**References**

[1] Padhi, A. K.; Nanjundaswamy, K. S.; Goodenough, J. B. Phospho-olivines as Positive-Electrode Materials for Rechargeable Lithium Batteries. J. Electrochem. Soc., 144 (1997) 1188-1194.

[2] Yamada, A.; Kudo, Y.; Liu, K.-Y. Phase Diagram of $Li_xMn_yFe_{1-y}PO_4$ ($0 \le x,y \le 1$). J. Electrochem. Soc., 148 (2001) A1153-A1158.

[3] Yamada, A.; Chung, S.-C. Crystal Chemistry of the Olivine-Type $Li(Mn_yFe_{1-y})PO_4$ and $(Mn_yFe_{1-y})PO_4$ as Possible 4 V Cathode Materials for Lithium Batteries. J. Electrochem. Soc., 148 (2001) A960-A967.

[4] Yamada, A.; Takei, Y.; Koizumi, H.; Sonoyama, N.; Kanno, R. Electrochemical, Magnetic, and Structural Investigation of the $Li_x(Mn_yFe_{1-y})PO_4$ Olivine Phases. Chem. Mater., 18 (2006) 804-813.

[5] Malik, R.; Zhou, F.; Ceder, G. Phase diagram and electrochemical properties of mixed olivines from first-principles calculations. Phys. Rev. B., 79 (2009) 214201.

[6] Roberts, M. R.; Vitins, G.; Denuault, G.; Owen, J. R. High Throughput Electrochemical Observation of Structural Phase Changes in $LiFe_{1-x}Mn_xPO_4$ during Charge and Discharge. J. Electrochem. Soc., 157 (2010) A381-A386.

[7] Bramnik, N. N.; Bramnik, K. G.; Nikolowski, K.; Hinterstein, M.; Baehtz, C.; Ehrenberg, H. Synchrotron Diffraction Study of Lithium Extraction from $LiMn_{0.6}Fe_{0.4}PO_4$. Electrochem. Solid-State Lett., 8 (2005) A379-A381.

[8] Nam, K.-W.; Yoon, W.-S.; Zaghib, K.; Chung, K. Y.; Yang, X.-Q. The phase transition behaviors of $Li_{1-x}Mn_{0.5}Fe_{0.5}PO_4$ during lithium extraction studied by in situ X-ray absorption and diffraction techniques. Electrochem. Commun., 11 (2009) 2023–2026.

[9] Kosova, N.V.; Devyatkina, E.T.; Ancharov, A.I.; Markov, A.V.; Karnaushenko, D.D.; Makukha, V.K. Structural studies of nanosized $LiFe_{0.5}Mn_{0.5}PO_4$ under cycling by in situ synchrotron diffraction. Solid State Ionics., 225 (2012) 564–569.

[10] Ravnsbæk, D. B.; Xiang, K.; Xing, W.; Borkiewicz, O. J.; Wiaderek, K. M.; Gionet, P.; Chapman, K. W.; Chupas, P. J.; Chiang, Y.-M. Extended Solid Solutions and Coherent Transformations in nanoscale Olivine Cathodes. Nano Lett., 14 (2014) 1484−1491.

[11] Tang, P.; Holzwarth, N. A. W. Electronic structure of $FePO_4$ , $LiFePO_4$, and related materials. Phys. Rev. B., 68 (2003) 165107.

[12] Osorio-Guillén, J.M.; Holm, B.; Ahuja, R.; Johansson, B. A theoretical study of olivine $LiMPO_4$ cathodes. Solid State Ionics., 167 (2004) 221-227.

[13] Nishimura, S.; Kobayashi, G.; Ohoyama, K.; Kanno, R.; Yashima, M.; Yamada, A. Experimental visualization of lithium diffusion in $Li_xFePO_4$. Nat. Mater., 7 (2008) 707-711.

[14] Rousse, G.; Rodriguez-Carvajal, J.; Patoux, S.; Masquelier, C. Magnetic structures of the triphylite $LiFePO_4$ and of its delithiated form $FePO_4$. Chem. Mater., 15 (2003) 4082–4090.

[15] Andersson, A. S.; Kalska, B.; Häggström, L.; Thomas, J. O. Lithium extraction/insertion in $LiFePO_4$: an X-ray diffraction and Mössbauer spectroscopy study. Solid State Ionics., 130 (2000) 41-52.

[16] Delacourt, C.; Rodríguez-Carvajal, J.; Schmitt, B.; Tarascon, J.-M.; Masquelier, C. Crystal chemistry of the olivine-type $Li_xFePO_4$ system ($0 \leq x \leq 1$) between 25 and 370 °C. Solid State Sci., 7 (2005) 1506-1516.

[17] Yamada, A.; Koizumi, H.; Nishimura, S.; Sonoyama, N.; Kanno, R.; Yonemura, M.; Nakamura, T.; Kobayashi, Y. Room-temperature miscibility gap in $Li_xFePO_4$. Nat. Mater., 5 (2006) 357-360.

[18] Andersson, A.S; Thomas, J.O. The source of first-cycle capacity loss in $LiFePO_4$. J. Power Sources, 97-98 (2001) 498-502.

[19] Roberts, M.; Biendicho, J. J.; Hull, S.; Beran, P.; Gustafsson, T.; Svensson, G.; Edström, K. Design of a new lithium ion battery test cell for in situ neutron diffraction measurements. J. Power Sources, 226 (2013) 249-255.

[20] Palatinus, L. PETS – program for analysis of electron diffraction data. Prague: Institute of Physics of the AS CR, 2011.

[21] Petricek, V.; Dusek, M.; Palatinus, L. Crystallographic Computing System JANA2006: General Features. Z. Kristallogr., 229 (2014) 345–352.

[22] Fisher, C. A. J.; Islam, M. S. Surface structures and crystal morphologies of $LiFePO_4$: relevance to electrochemical behavior. J. Mater. Chem., 18 (2008) 1209–1215.

[23] Cottrell, F.G. Residual current in galvanic polarization, regarded as a diffusion problem. Z. Phys. Chem., 42 (1903) 385-431.

[24] Montella, C. Discussion of the potential step method for the determination of the diffusion coefficients of guest species in host materials Part I. Influence of charge transfer kinetics and ohmic potential drop. J. Electroanal. Chem., 518 (2002) 61-83.

[25] Vorotyntsev, M. A.; Levi, Mikhael D.; Aurbach, D. Spatially limited diffusion coupled with ohmic potential drop and/or slow interfacial exchange: a new method to determine the diffusion time constant and external resistance from potential step (PITT) experiments. J. Electroanal. Chem., 572 (2004) 299–307.

[26] Meethong, N.; Kao, Y.-H.; Carter, W. C.; Chiang, Y.-M. Comparative Study of Lithium Transport Kinetics in Olivine Cathodes for Li-ion Batteries. Chem. Mater., 22 (2010) 1088–1097.

[27] Hadermann, J.; Abakumov, A.M.; Turner, S.; Hafideddine, Z. ; Khasanova, N.R.; Antipov, E.V.; Van Tendeloo, G. Solving the Structure of Li Ion Battery Materials with Precession Electron Diffraction: Application to $Li_2CoPO_4F$. Chem. Mater., 23 (2011) 3540–3545.

[28] Hadermann, J.; Abakumov, A., Van Rompaey, S.; Perkisas, T.; Filinchuk, Y.; Van Tendeloo, G. Crystal structure of a lightweight borohydride from submicrometer crystallites by precession electron diffraction. Chem. Mater., 24 (2012) 3401-3405.

[29] Gemmi, M.; Oleynikov, P. Scanning reciprocal space for solving unknown structures: energy filtered diffraction tomography and rotation diffraction tomography methods. Z. Kristallogr., 228 (2013) 51-58.

[30] Kope¢, M.; Yamada, A.; Kobayashi, G.; Nishimura, S.; Kanno, R.; Mauger, A.; Gendron, F.; Julien, C.M. Structural and magnetic properties of $Li_x(Mn_yFe_{1-y})PO_4$ electrode materials for Li-ion batteries. J. Power Sources, 189 (2009) 1154–1163.

[31] Mishima, Y.; Hojo, T.; Nishio, T.; Sadamura, H.; Oyama, N.; Moriyoshi, C.; Kuroiwa, Y. MEM Charge Density Study of Olivine $LiMPO_4$ and $MPO_4$ (M = Mn, Fe) as Cathode Materials for Lithium-Ion Batteries. J. Phys. Chem. C., 117 (2013) 2608−2615.

[32] Bramnik, N. N.; Nikolowski, K.; Baehtz, C.; Bramnik, K. G.; Ehrenberg, H. Phase Transitions Occurring upon Lithium Insertion-Extraction of $LiCoPO_4$. Chem. Mater., 19 (2007) 908-915.

[33] Kosova, N. V.; Podgornova, O. A.; Devyatkina, E. T.; Podugolnikov, V. R.; Petrov, S. A. Effect of $Fe^{2+}$ substitution on the structure and electrochemistry of $LiCoPO_4$ prepared by mechanochemically assisted carbothermal reduction. J. Mater. Chem. A, 2 (2014) 20697-20705.

[34] Ni, J.; Han, Y.; Gao, L.; Lu, L. One-pot synthesis of CNT-wired $LiCo_{0.5}Mn_{0.5}PO_4$ nanocomposites. Electrochem. Commun., 31 (2013) 84–87.

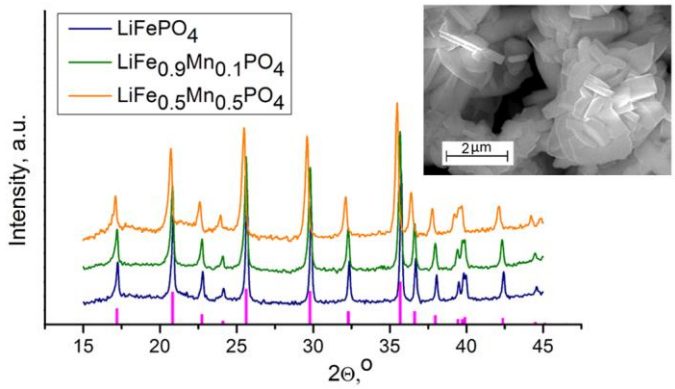


**Figure 1.** XRPD patterns of $LiFePO_4$, $LiFe_{0.9}Mn_{0.1}PO_4$ and $LiFe_{0.5}Mn_{0.5}PO_4$; calculated peaks of $LiFePO_4$ are also included (ICDD PDF #83-2092). Typical SEM image of the obtained samples (shown representatively for $LiFePO_4$) is at the inset.

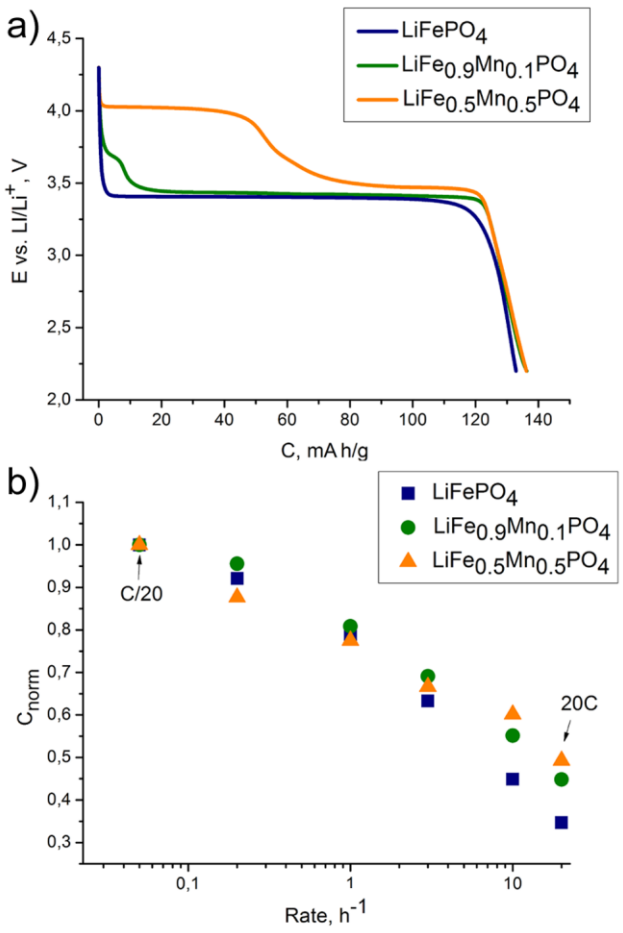


**Figure 2.** Discharge curves at 0.05C rate (a) and normalized C-rate dependence (b) for the studied samples.

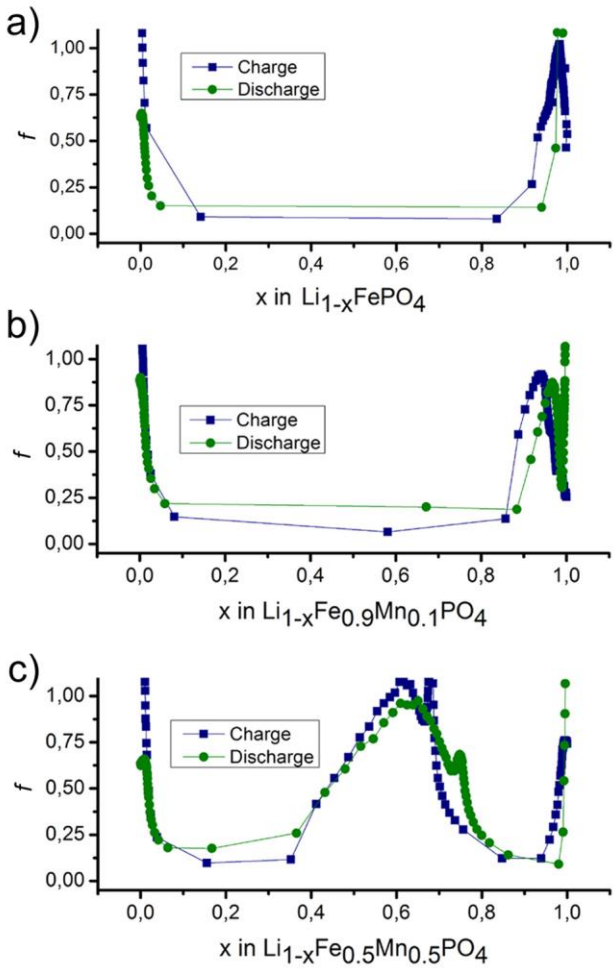


**Figure 3.** *f* - *x* dependence for $Li_{1-x}FePO_4$ (a), $Li_{1-x}Fe_{0.9}Mn_{0.1}PO_4$ (b) and $Li_{1-x}Fe_{0.5}Mn_{0.5}PO_4$ (c).

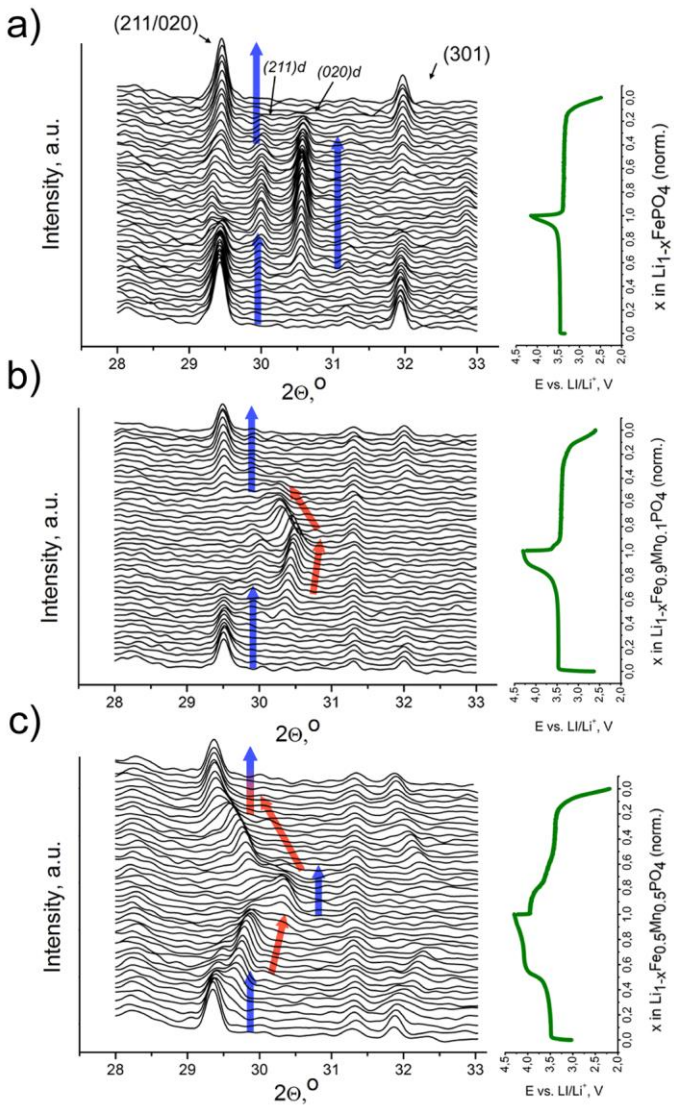


**Figure 4.** Selected region of the *in situ* XRPD patterns for $Li_{1-x}FePO_4$ (a), $Li_{1-x}Fe_{0.9}Mn_{0.1}PO_4$ (b) and $Li_{1-x}Fe_{0.5}Mn_{0.5}PO_4$ (c). Blue arrows correspond to x values for which no significant shift of diffraction peaks was observed (two-phase mechanism); red arrows – to solid solution regions. Peaks of the delithiated phase are marked with "d"

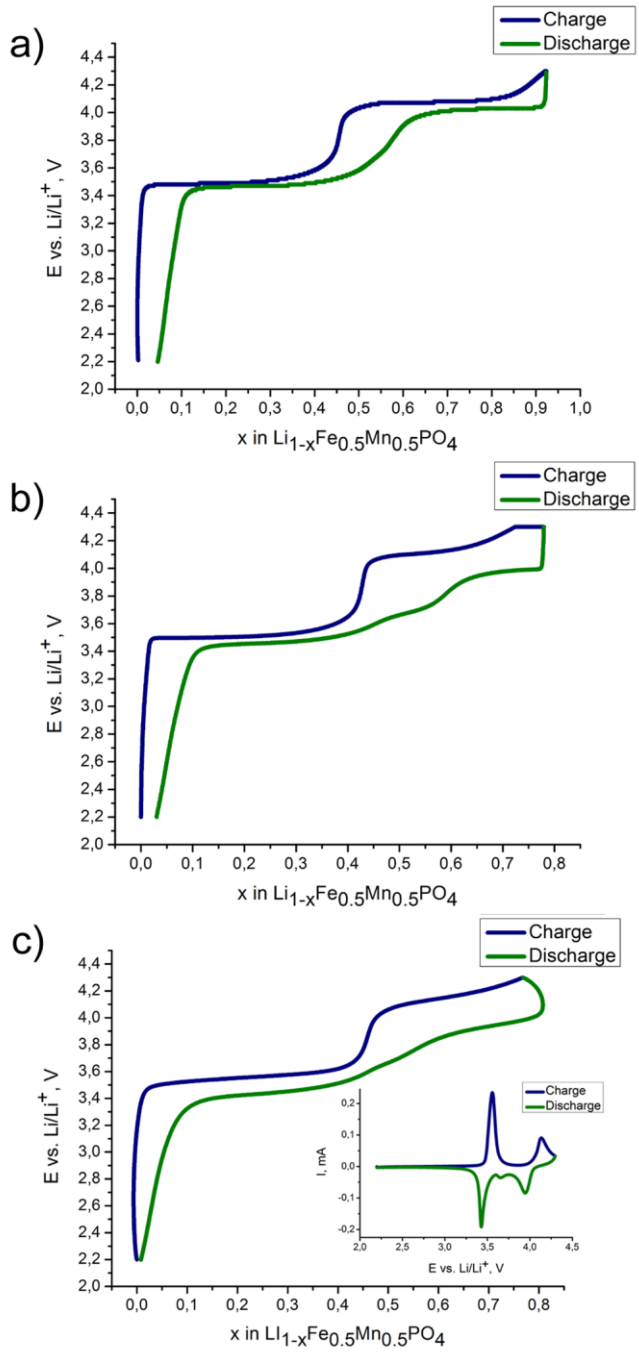


**Figure 5.** E-x dependence for $Li_{1-x}Fe_{0.5}Mn_{0.5}PO_4$ obtained from PITT (a), GCPL at 0.2C rate (b) and CV collected at 50 μV $s^{-1}$ scan rate (c). CV curve is at the inset

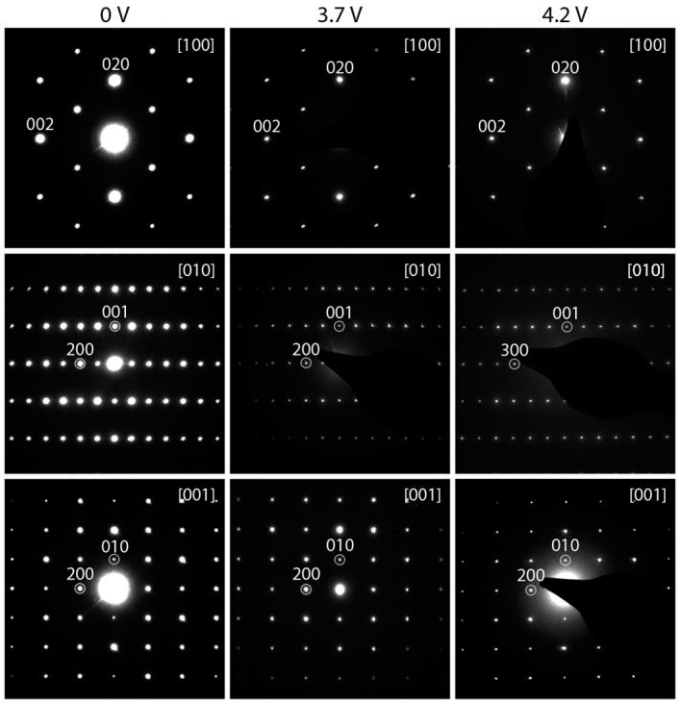


**Figure 6**. Main zone axis SAED patterns for the pristine $LiFe_{0.5}Mn_{0.5}PO_4$ sample and the $Li_{1-x}Fe_{0.5}Mn_{0.5}PO_4$ samples charged to 3.7 V and 4.2 V vs. $Li/LI^+$.

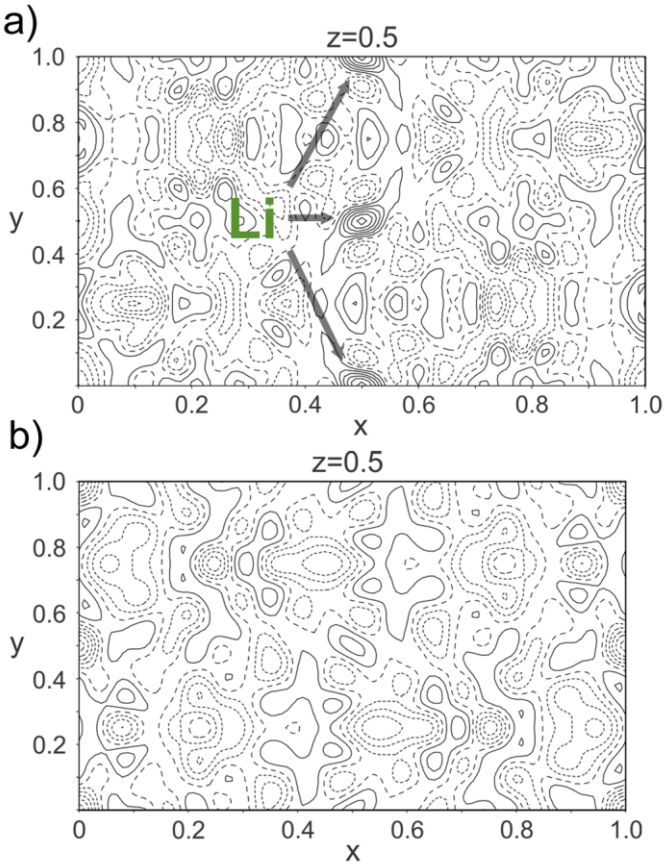


**Figure 7**. Difference Fourier map around the Li position for the $LiFe_{0.5}Mn_{0.5}PO_4$ (a) and $Li_{0.1}Fe_{0.5}Mn_{0.5}PO_4$ (b) structures, calculated from EDT data. Note the presence of a clear maximum of scattering density in the first case and its absence in the second case

**Table 1.** Results of XRPD and EDX studies of as-prepared $LiFe_{1-y}Mn_yPO_4$, y = 0, 0.1, 0.5

| | $LiFePO_4$ | $LiFe_{0.9}Mn_{0.1}PO_4$ | $LiFe_{0.5}Mn_{0.5}PO_4$ |
|---|---|---|---|
| a, Å | 10.301(1) | 10.318(1) | 10.371(2) |
| *b*, Å | 5.990(1) | 6.000(1) | 6.036(1) |
| *c*, Å | 4.6801(5) | 4.6869(8) | 4.7108(9) |
| V, $Å^3$ | 288.81(4) | 290.21(6) | 294.92(7) |
| Fe:Mn ratio | - | 0.91(2):0.09(2) | 0.54(2):0.46(2) |

**Table 2.** Average $f_{sum}$ values for the PITT experiment in 2.2-4.3 V vs. $Li/Li^+$ potential range

| | $LiFePO_4$ | $LiFe_{0.9}Mn_{0.1}PO_4$ | $LiFe_{0.5}Mn_{0.5}PO_4$ |
|---|---|---|---|
| $f_{charge}$ | 0,10 | 0,19 | 0,39 |
| $f_{discharge}$ | 0,22 | 0,26 | 0,42 |